electronics

MDPI

Article

A Novel High-Gain Dual-Beam Circularly Polarized Antenna Array Based on Anti-Phase Field Distribution in Epsilon-Near-Zero (ENZ)

Dan Long * and Rulong He *

Naval University of Engineering, Wuhan 430033, China
* Correspondence: 0909031056@nue.edu.cn (D.L.); 0909031043@nue.edu.cn (R.H.)

Abstract

Dual-beam circularly polarized antenna arrays are widely demanded in high-capacity wireless and satellite communication systems. However, conventional designs typically suffer from complex feeding networks, large profile, and high insertion loss, which limit their integration level and efficiency. To address these issues, this paper proposes a low-loss, highly integrated dual-beam circularly polarized antenna array based on a substrate-integrated waveguide equivalent ENZ feeding network. A new physical phenomenon is revealed that the tangential electric field in the slots exhibits an equal-amplitude and anti-phase distribution due to the combined effect of the uniform field distribution in the ENZ medium and the boundary conditions of the slotted perfect electric conductor. Using this inherent mechanism, the antenna achieves symmetric dual-beam radiation at approximately $\pm 27^{\circ}$ in the E-plane. A polarization conversion meta surface layer is loaded to convert linear polarization into circular polarization. A prototype is fabricated and measured. At 8.3 GHz, the measured peak gain is 9.1 dBi, the minimum axial ratio is better than 1.5 dB, and the radiation efficiency is higher than 85%. The proposed array features simple structure, low loss, and high integration. Compared with conventional feeding structures, it eliminates the need for additional phase shifters or power dividers, effectively reducing insertion loss and structural complexity. It exhibits good application potential in compact base stations and satellite communication terminals.

Keywords: antenna array; circular polarization; dual-beam radiation; epsilon-near-zero (ENZ); substrate integrated waveguide (SIW); low-loss feeding

1. Introduction

With the rapid development of 5G, 6G, low-earth-orbit satellite constellations, and high-capacity multi-user communication systems, dual-beam circularly polarized (CP) antenna arrays have become critical components [1–9]. Dual-beam antennas can cover multiple spatial directions simultaneously [10,11], supporting efficient multi-user transmission. Circular polarization effectively reduces multipath fading and polarization mismatch in complex propagation environments [12–14]. Therefore, it is of great significance to develop high-gain, low-loss, compact, and highly integrated dual-beam CP antenna arrays for future wireless communication terminals.

However, traditional dual-beam CP antenna arrays rely heavily on complex feeding networks, such as Butler matrices, multi-stage power dividers, or series-fed structures with precise phase control [8,15]. These schemes inevitably lead to bulky structures, high

Check for updates

Received: 12 May 2026
Revised: 13 June 2026
Accepted: 18 June 2026
Published: 22 June 2026

Copyright: © 2026 by the authors. Licensee MDPI, Basel, Switzerland. This article is an open access article distributed under the terms and conditions of the Creative Commons Attribution (CC BY) license.

insertion loss, low efficiency, and difficult integration. Although they can achieve dual-beam radiation, their bulky feeding networks significantly limit performance and practical application in compact systems.

ENZ materials have attracted extensive attention in antenna feeding networks due to their unique electromagnetic properties: nearly constant phase, uniform field distribution [3,16–18], and low transmission loss [19–22]. ENZ-based feeding structures can achieve in-phase and equal-amplitude excitation without complex power division networks, showing obvious advantages in miniaturization and low-loss design. However, most reported ENZ antennas are limited to linear polarization and single-beam radiation. More importantly, the field distribution mechanism inside the radiating slots of ENZ feeding networks—which directly determines multi-beam radiation performance—has not been thoroughly studied.

Several recent works have exploited the unique field behaviors of ENZ structures for different radiation functions. For instance, Liu et al. [23] reported a low-profile ENZ cavity array where the internal electric field exhibits a sign-function-like distribution to broaden the beamwidth for wide-angle beam scanning. Dadgarpour et al. [24] demonstrated an ENZ-based dual-beam antenna by using anisotropic ENZ meta-lens arrays to route the radiated energy into two symmetric directions. However, that design relies on external wave-manipulation elements and achieves only linear polarization. In contrast, this work reveals a distinct physical mechanism: under the combined effect of the uniform ENZ field and the boundary condition of a slotted perfect electric conductor (PEC), the tangential electric field inside the slots naturally presents an equal-amplitude and anti-phase distribution. Consequently, symmetric dual beams are directly excited without any additional phase shifters, power dividers, or external wave-routing structures. This feature fundamentally differs from the beam-scanning application in [23] and the meta-lens dependent scheme in [24].

To fill the above gaps, this paper proposes a novel low-loss dual-beam CP antenna array using an SIW-based ENZ feeding network. The core innovation lies in a system-integration scheme that synergistically combines an SIW-based ENZ feeding network with uniform in-phase excitation, the inherent anti-phase tangential-field distribution on the slotted PEC surface that directly generates symmetric dual-beam radiation, and a polarization-conversion meta surface layer that transforms the linear-polarized dual beams into circular polarization.

This integrated three-layer architecture eliminates the need for complex beamforming networks and achieves low-profile, high-efficiency CP dual-beam radiation. A prototype is fabricated and measured. At 8.3 GHz, the proposed antenna achieves a peak gain of 9.1 dBi, a minimum axial ratio below 1.5 dB, and a radiation efficiency higher than 85%. To quantitatively illustrate the low-loss advantage of the proposed ENZ-based feeding network, we compare its excess insertion loss with that of conventional Butler matrices. Here, excess insertion loss is defined as the measured loss beyond the theoretical 6 dB splitting loss for a 1-to-4 power division. Our ENZ network exhibits an excess insertion loss of approximately 0.9 dB. In comparison, typical 4×4 Butler matrices reported in the literature have excess insertion losses ranging from 2 dB to 4 dB [8], mainly due to the accumulated losses of hybrid couplers, crossover structures, and phase shifters. This quantitative comparison highlights the intrinsic low-loss characteristic of the proposed architecture, making it particularly attractive for compact, high-efficiency communication terminals.

2. Design of Antenna Structure

The proposed antenna adopts a three-layer stacked configuration along the z-axis, which is beneficial to miniaturization and high integration as shown in Figure 1. The first

layer is a single-row substrate integrated waveguide (SIW) operating at its cutoff frequency to realize the equivalent ENZ characteristic, which can generate a uniform electric field distribution to provide stable feeding for the radiation elements. The second layer is composed of four parallel SIW rows with the same structural parameters as the first layer, ensuring the same ENZ resonant frequency and high-efficiency energy coupling between layers. The third layer is a polarization conversion meta surface composed of metallic patches loaded on a dielectric substrate, which is used to convert linear polarization into circular polarization and improve the gain and directivity of the dual beams.

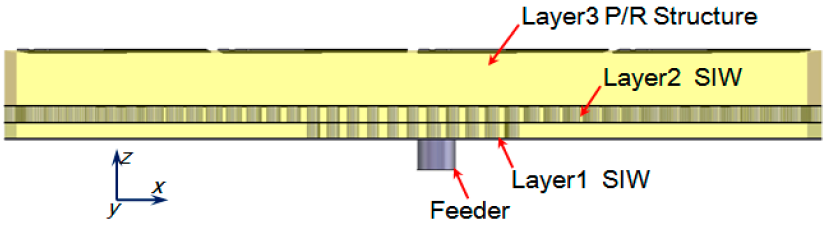


Figure 1. Schematic of the three-layer antenna structure.

The antenna is fed by a coaxial probe at the bottom, and good impedance matching can be achieved by adjusting the probe position. The thicknesses of the first, second, and third layers are 0.5 mm, 0.5 mm, and 2 mm, respectively. The dielectric substrate used for all three layers is Rogers RO6002, with a loss tangent tanδ = 0.0015 [25].

When the input frequency satisfies the ENZ resonance condition of the SIW, the first layer exhibits a uniform field distribution, which is then coupled to the four parallel SIW rows in the second layer. As a result, the radiating slots on the second layer are excited uniformly and in-phase, generating linearly polarized dual-beam radiation. After passing through the polarization conversion layer, the linearly polarized dual beams are converted into circularly polarized waves and radiate into space. Figure 2 is the schematic diagram of the overall antenna configuration.

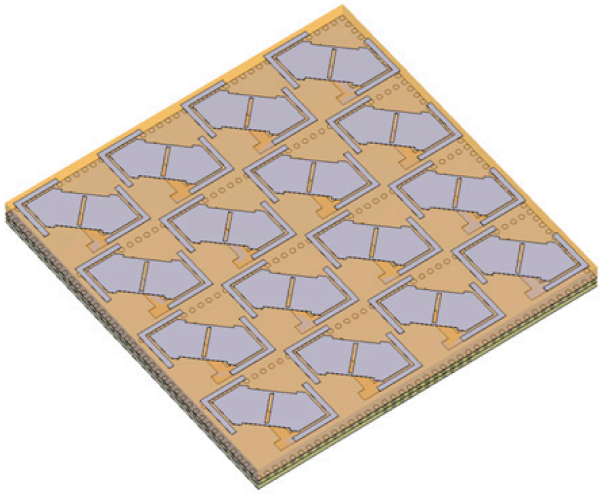


Figure 2. The schematic diagram of the overall antenna configuration.

3. Design of the SIW-Based ENZ Feeding Network

This section presents the design of the substrate integrated waveguide (SIW)-based ENZ feeding network, which provides uniform excitation and forms symmetric dual-beam radiation. The first-layer SIW structure is depicted in Figure 3, where the key geometrical parameters include the radius of metallic vias R, the center-to-center spacing between adjacent vias s, and the distance between the two via rows w (where $w \leq 1/20\ \lambda_g$, and λ_g is the guided wavelength within the SIW). The SIW can be equivalent to a rectangular

waveguide with an effective broadside width w_{eff}, which is calculated by the empirical formula widely used in SIW designs [26].

$$w_{\text{eff}} = \frac{2w}{\pi}\arctan\left(\frac{\pi s}{4w}\ln\frac{s}{4R}\right), \quad (1)$$

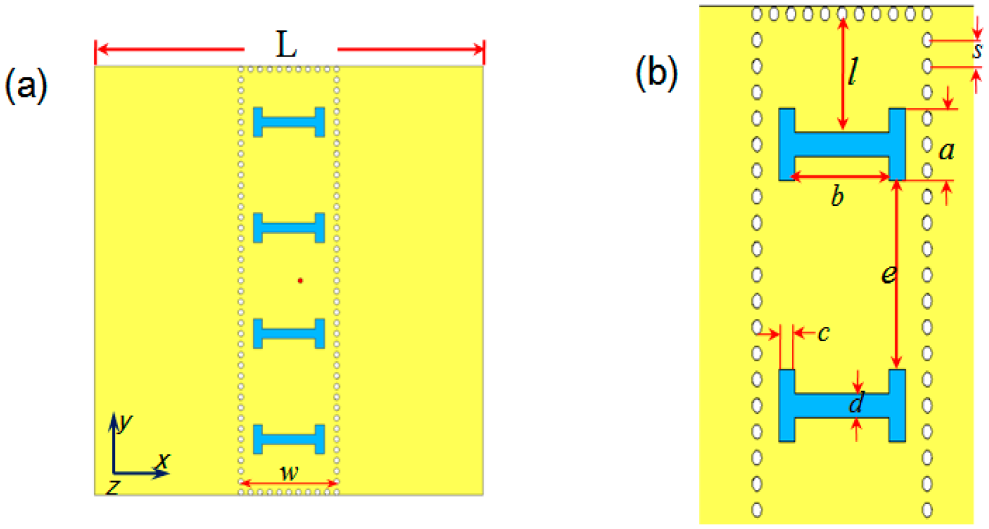


Figure 3. Schematic diagram of the first-layer SIW structure and the ENZ feeding network. (**a**) The SIW surface is etched with four equally spaced radiating slots. (**b**) Detailed geometrical dimensions of the SIW structure.

In the TE_{10} mode, the effective permittivity ε_{eff} of the waveguide can be characterized by the Drude dispersion model [27] and is expressed as

$$\varepsilon_{\text{eff}}(f) = \varepsilon_r - c^2/(4w_{eff}^2 f^2) \quad (2)$$

where c is the speed of light in free space, f is the operating frequency of the SIW, and ε_r is the relative permittivity of the substrate. When ε_{eff} is 0, the SIW operates in the ENZ mode, exhibiting a near-zero propagation constant and an infinite guided wavelength. The corresponding operating frequency (f) can be calculated as the cutoff frequency.

Subsequently, four identical radiating slots are etched on the top surface of the SIW. The geometry and dimensions of a single radiating slot are depicted in Figure 3b. In this work, the detailed parameters of the ENZ feeding network are listed in Table 1.

Table 1. Detailed parameters of the ENZ feeding network.

Parameter	Value (mm)	Parameter	Value (mm)
L	43.8	b	6
w	10.8	c	1
l	5.2	d	1
s	1.08	e	7.8
a	3		

When the SIW is excited by a coaxial probe, the field distribution under the ENZ mode is illustrated on the left side of Figure 3a. Due to the infinite guided wavelength within the ENZ medium, the internal electric field is uniformly distributed with negligible phase variation, thereby achieving in-phase radiation at the four radiating slots.

Subsequently, another SIW (layer 2) is stacked on top of the first layer as shown in Figure 4a. In Figure 4a, the layer 2 consists of four SIWs arranged side by side, which are identical to those in the first layer, but oriented orthogonally to the first-layer structure. The

rationale behind this combined configuration lies in exploiting the uniform electric field characteristic inherent in the ENZ medium. First, a uniform field distribution is achieved within the first-layer SIW. Consequently, its four slots act as feeding sources with equal amplitude and phase. Due to the structural similarity between the first and second SIW layers, impedance matching is achieved between the layers. Through coupling, the field distribution is transferred, ultimately establishing a uniform field across the four parallel slotted rows in the second layer. All full-wave simulations were carried out using CST Microwave Studio 5.0. This results in a 16-element feeding array with equal amplitude and phase as shown in Figure 4b.

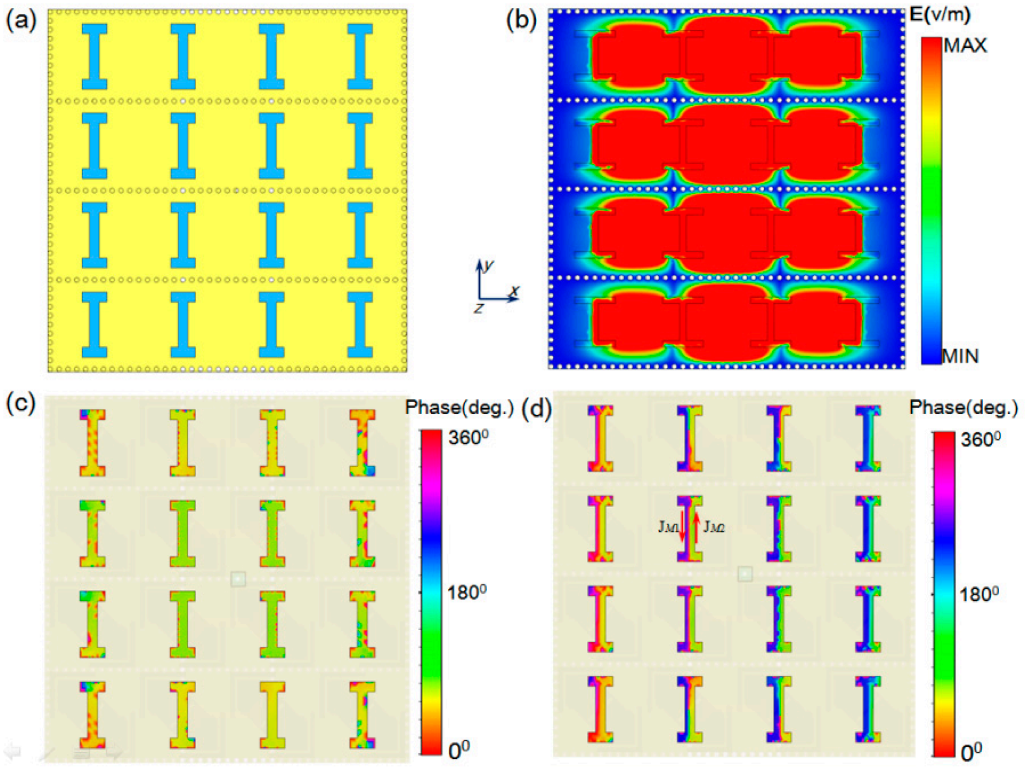


Figure 4. Overall electric field distribution and electric field distribution within the slots in the second layer of the SIW feeding network. (**a**) Schematic diagram of the second-layer SIW structure. (**b**) A uniform electric field distribution is exhibited within the four SIWs arranged side by side at cutoff frequency. (**c**) Phase of the electric field along the z-direction (normal direction) within the slots on the SIW surface. (**d**) Phase of the electric field along the x-direction (tangential direction) within the slots on the SIW surface.

Figure 4c demonstrates that all electric field components perpendicular to the slots in the second layer are uniform. Notability, an anti-phase symmetry phenomenon is observed for the horizontal electric fields on the slot surfaces.

Under the ENZ condition, the effective permittivity ε_{eff} of the SIW satisfies near zero. From $\nabla \times \mathbf{H} = j\omega\varepsilon_{eff}\mathbf{E}$, the electric field of E in the SIW becomes irrotational, leading to a uniform distribution along the slot length (y-axis). For a narrow slot (width of $d \ll \lambda g$) etched on a perfect electric conductor (PEC), the tangential electric field of $\mathbf{E}_x(y)$ must satisfy the boundary condition that its line integral around a loop crossing the slot vanishes.

$$\int_{-\frac{b}{2}}^{\frac{b}{2}} E_x(y)dy = 0 \tag{3}$$

and $E_x(\pm\frac{b}{2}) = 0$ at the metal edges. Expanding $\mathbf{E}_x(y)$ in a Fourier sine series automatically satisfies $E_x(\pm\frac{b}{2}) = 0$:

$$E_x(y) = \sum_{n=1}^{\infty} a_n \sin(\frac{2n\pi y}{b}) \tag{4}$$

The line integral condition is automatically satisfied because each sine term integrates to zero over the symmetric interval. The fundamental mode (n = 1) is odd-symmetric and has the longest spatial period. Higher-order modes ($n \geq 2$) have cutoff frequencies proportional to n/d. Because of the $d \ll \lambda g$, these modes are evanescent and their amplitudes decay exponentially away from the slot. Hence, the mode of n = 1 dominates, leading to an equal-amplitude, anti-phase distribution. This is confirmed by the simulated field profile which shows a clear odd-symmetric distribution across the slot and the field is equivalent to two parallel but opposite magnetic currents as shown in Figure 4d.

The far-field radiation pattern of a single such slot can be derived from the equivalence principle. The anti-phase tangential field corresponds to two equivalent magnetic currents J_M and $-J_M$ separated by the slot width. For a slot located at the origin, the far-zone electric field is proportional to the spatial synthesis of the pair of equivalent opposite magnetic current source inside the slot, which can expressed as

$$E_{far}(\theta) \propto \int_{-\frac{b}{2}}^{\frac{b}{2}} E_x(y) e^{jkr\sin\theta} dy \tag{5}$$

Substituting the odd-symmetric fundamental mode $E_x(y) = E_0\sin(2\pi y/b)$ which exhibits $E_{far}(\theta)$ is minimum at $\theta = 0^0$ and two symmetric peaks at angles $\theta = \pm\theta_m$. For the present parameters (b = 6 mm at 8.233 GHz), numerical calculation gives the peak directions at $\theta_m \approx \pm 30^\circ$.

Four slots are spaced by distance e = 7.8 mm along the y-axis. The array factor for four slots with alternating phases is given by

$$AF(\theta) = \sum_{i=1}^{4} (-1)^{i+1} e^{jk(i-1)e\sin\theta} \tag{6}$$

Because the SIW behaves as an ENZ medium, the four slots are excited with equal amplitude and in-phase (i.e., the excitation phases across different slots are identical). However, within each slot, the tangential electric field exhibits an odd-symmetric distribution (equal amplitude and opposite phase on the two halves of the slot), as shown in the simulated field profile in Figure 4d. This odd-symmetric distribution is equivalent to two opposite magnetic currents (illustrated in Figure 4d). Consequently, the effective radiation from adjacent slots has a 180° phase difference, leading to the alternating-sign term $(-1)^{i+1}$ in the array factor. The phase distribution plotted in Figure 4d further confirms the anti-phase behavior across the slot. This factor further suppresses the sidelobes and sharpens the main beams and the beam direction can be reduced to about 30°.

At present, this anti-phase tangential field distribution in slotted ENZ waveguides and its direct application to dual-beam antenna design has not been reported in the open literature. The physical insight presented here not only explains the underlying operation of the proposed antenna but also provides a generalizable approach for developing compact multi-beam radiating systems.

Figure 5 presents the S_{11} of the SIW feeding network. As depicted in Figure 5, the feeding network exhibits two resonant frequencies, located at 8.233 GHz and 8.502 GHz, respectively. Among these, 8.233 GHz corresponds to the resonance point at which the network operates in the ENZ mode. In contrast, the resonance depth of the ENZ mode is

far stronger than that of the F-P mode. It is evident that when operating in the ENZ mode, the feeding network is capable of effectively radiating electromagnetic waves.

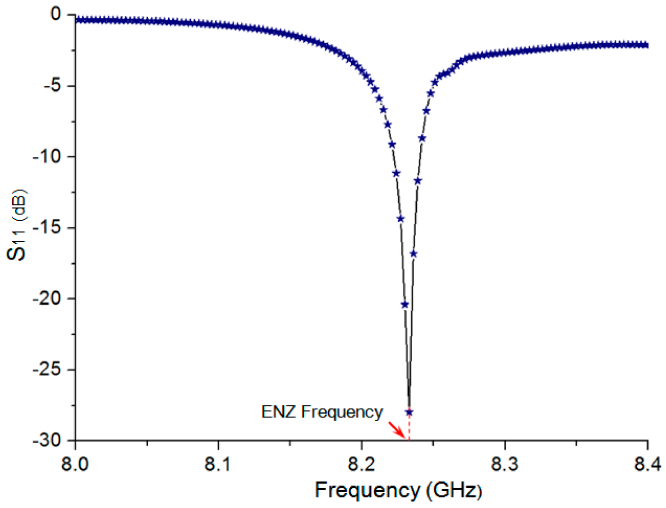


Figure 5. Simulated S_{11} of the SIW feeding network.

Figure 6 shows the far-field radiation gain pattern in the E-plane and the three-dimensional gain pattern of the SIW feeding network operating in the ENZ mode. The patterns exhibit two prominent and symmetric beams. However, The two lobes are not highly independent; each has a beam direction of approximately 30° which agrees well with the numerical calculation. The radiation is linearly polarized, and the maximum gain is about 7.83 dBi.

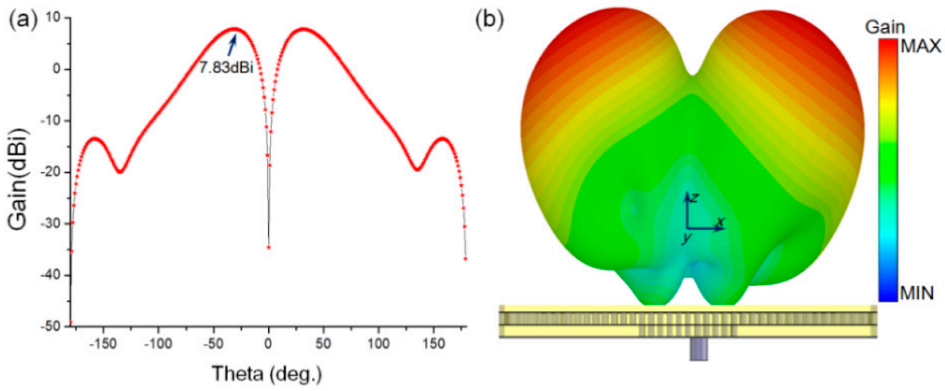


Figure 6. Far-field gain patterns of the SIW feeding network in ENZ mode: (**a**) gain pattern in the plane (E-plane), (**b**) three-dimensional pattern.

4. Design of Polarization Conversion and Radiating Structure

To further increase the gain of the two beams and realize circular polarization, a polarization conversion layer is integrated on top of the feeding network, as illustrated in Figure 7. The corresponding parameters of the polarization conversion layer are listed in Table 2.

By introducing asymmetry in the surface impedance, polarization rotation of the reflected or transmitted wave can be achieved [28]. Figure 7b illustrates the structure of the polarization-rotating meta surface (PRMS). It consists of a dielectric substrate and an upper-layer meta surface metallic patch, where the meta surface patch is a square metallic patch with a 45° inclined slit etched at its center. The polarization rotation characteristics can be observed through the amplitude and phase of the reflection coefficients as shown in Figure 8. Assuming a TM wave incident normally along the *z*-axis onto the PRMS

surface ($T_{TE/TM}$ represents the polarization rotation ratio, i.e., the ratio of the transmitted TE wave orthogonal to the incident TM field), it is found that the magnitude of $T_{TM/TM}$ is below −10 dB from 7.5 GHz to 8.8 GHz, while $T_{TE/TM}$ exceeds −10 dB, indicating that the incident TM wave is primarily converted into an orthogonally polarized transmitted TE wave as depicted in Figure 8a. Furthermore, at the center frequency of 8.233 GHz, the phase of $T_{TE/TM}$ is approximately −90°, meaning that the incident TM wave leads the transmitted TE wave by 90°. In other words, the incident and transmitted waves exhibit a 90° polarization rotation accompanied by 90° phase difference, thereby generating a left-hand circularly polarized (LHCP) wave. In addition, the polarization sense can be tuned by reversing the orientation of the meta surface slit.

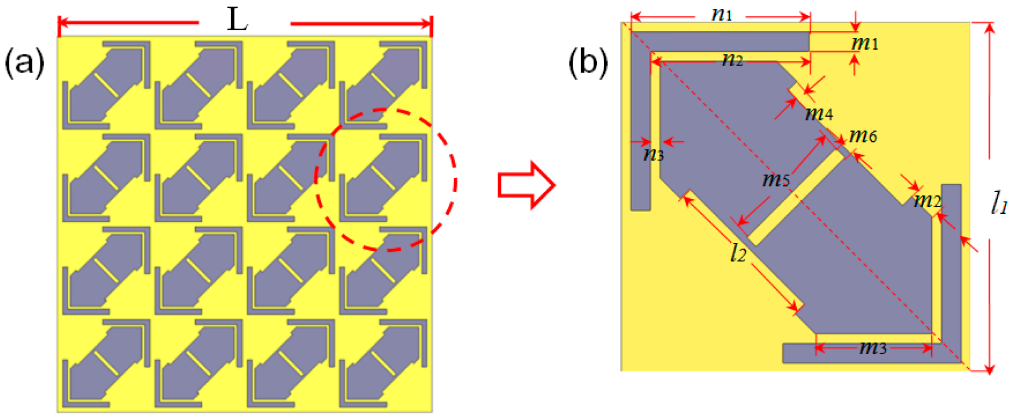


Figure 7. Polarization conversion and radiating layer. (**a**) Schematic diagram of the unit cell distribution on the surface. (**b**) Schematic diagram of a single unit cell with its parameters.

Table 2. Detailed parameters of Polarization Conversion and Radiating Structure.

Parameter	Value (mm)	Parameter	Value (mm)
l_1	11.4	l_2	5
m_1	0.6	m_2	0.9
m_3	3.6	m_4	0.3
m_5	3.9	m_6	0.4
n_1	5.5	n_2	4.9
n_3	0.3		

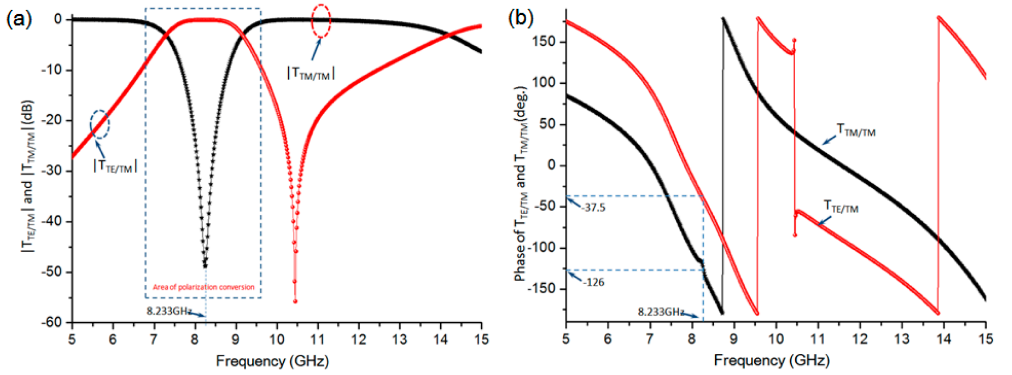


Figure 8. Schematic diagram of polarization conversion performance. (**a**) Transmission coefficient curves of the polarization conversion on radiating layer. (**b**) The polarization conversion phase.

Figure 9 shows the S_{11} of the entire antenna after covering the polarization conversion and radiation layer. It can be observed that at 8.3 GHz, when the antenna operates in the ENZ state, it radiates effectively while the inherent Fabry–Pérot resonant effect of the

SIW is effectively suppressed. Figure 10 illustrates the far-field radiation gain pattern (E-plane and H-plane) and the three-dimensional pattern of the antenna which is covered the polarization conversion and radiation layeroperating in ENZ mode. Figure 10a shows the simulated E-plane and H-plane radiation pattern at 8.3 GHz. Due to the alternating-phase excitation of the four slots, the H-plane pattern exhibits a broad beam with relatively low gain, as expected from the array factor. The E-plane pattern shows beam peaks at $-27.8°$ and $+26.7°$, demonstrating good symmetry and the maximum sidelobe appears at approximately $\pm 100°$ and is about 19 dB below the main lobe, meeting typical engineering requirements. Therefore, the dual-beam characteristic is primarily discussed in the E-plane. Nevertheless, the H-plane pattern confirms the absence of grating lobes and acceptable cross-polarization levels. Compared with Figure 6, the independence of the dual beams is significantly enhanced. The radiation exhibits circular polarization, and the maximum gain is increased to 9.1 dBi.

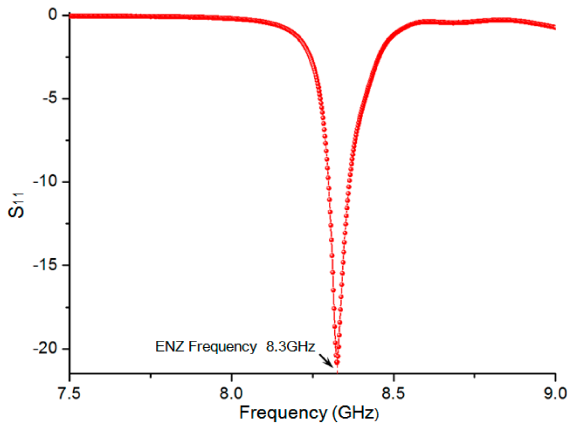


Figure 9. S_{11} of the entire antenna covered the polarization conversion and radiation layer.

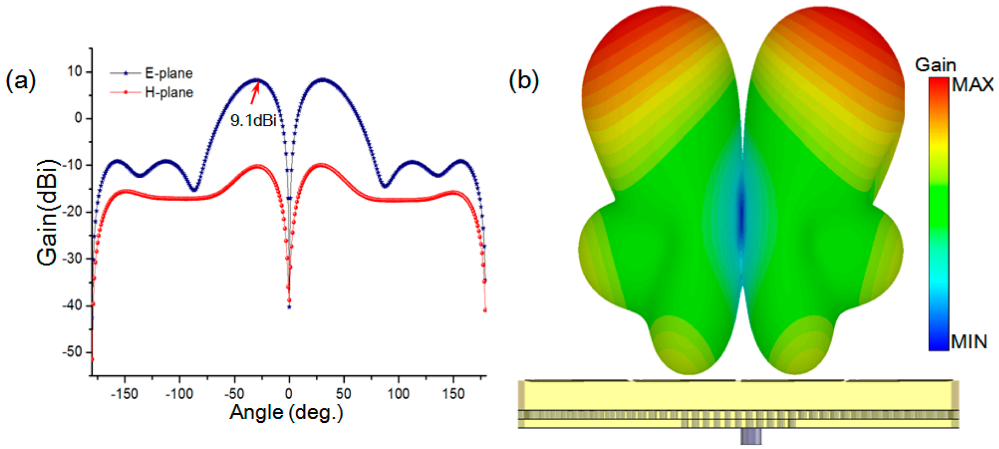


Figure 10. Radiation characteristics of the entire antenna covered the polarization conversion and radiation layer. (**a**) The far-field radiation gain pattern in the E-plane and H-plane of the whole structure. (**b**) The three-dimensional pattern of the whole structure.

Figure 11 shows the Simulated LHCP/RHCP gain pattern of the antenna. From the simulated LHCP/RHCP patterns, at the dual-beam peaks ($\approx \pm 27°$), the LHCP gain is about 9.1 dBi and the RHCP gain is about -10.2 dBi, giving an XPD of 17.2 dB. In the H-plane, the cross-polarization discrimination (XPD) is approximately 19.3 dB. These values indicate good circular polarization purity.

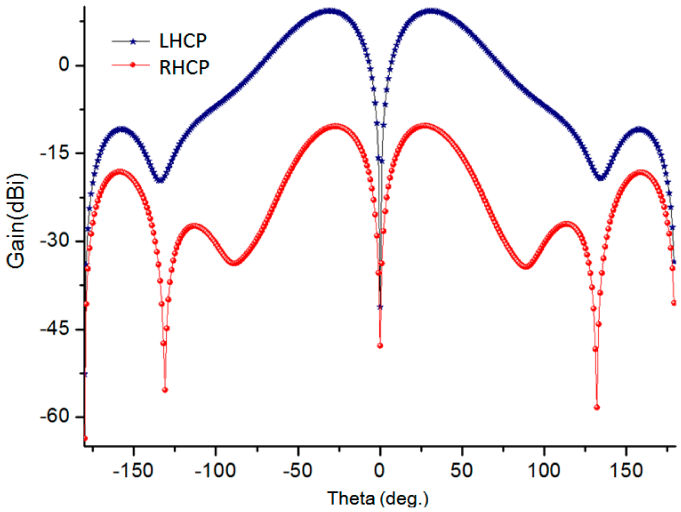


Figure 11. Simulated LHCP/RHCP gain pattern of the antenna.

5. Experimental Comparison and Measurement

Subsequently, a measurement and comparison experiment was conducted. The antenna was measured in an anechoic chamber using a Keysight N5225B vector network analyzer. The gain was measured using the comparison method with a standard-gain horn reference, yielding a peak gain of 9.1 dBi with an estimated uncertainty of ± 0.5 dB; axial ratio was measured using the rotating linear-polarization method, giving a minimum value of 1.5 dB with an uncertainty of ± 0.2 dB, radiation efficiency was extracted using the Wheeler cap method, reaching 85.3% (including dielectric, conductor, and polarization-conversion losses)at 8.3 GHz, the VNA was calibrated with SOLT, and the uncertainty for S_{11} is ± 0.2 dB. Based on the simulation model, a prototype antenna was designed and fabricated, as shown in Figure 12. Figure 13 presents the comparison S_{11} and E-plane radiation patterns between the measured data and the simulated data. It can be observed from Figure 13 that the measured results show good agreement with the simulated ones. In the S_{11} curve, the measurement verifies that the designed feeding network achieves ENZ resonant matching feeding. It is noted that, due to tolerances in design and fabrication accuracy, a slight frequency shift occurs compared to the simulated results as shown in Figure 13a which shows that the measured 10 dB return loss bandwidth ($|S_{11}| \leq -10$ dB) is approximately from 8.16 GHz to 8.41 GHz, corresponding to a relative bandwidth of 3.02%. Moreover, the measured and simulated radiation pattern curves exhibit the same variation trend with consistent gain as shown in Figure 13b. Comparing the simulated and measured axial ratio results, the axial ratio values at the resonant frequency are significantly lower than 3 dB and the 3 dB axial ratio bandwidth is approximately 2.9%, demonstrating that the antenna achieves circular polarization at the operating frequency as shown in Figure 13c. Figure 13 demonstrates that the proposed antenna is experimentally validated, and the measured results agree well with simulations. The measured 3 dB axial ratio bandwidth is approximately 2.9%, which is indeed relatively narrow for some wideband applications. This limitation mainly stems from the resonant nature of the polarization-conversion meta surface. Nevertheless, this bandwidth is still sufficient for narrowband satellite downlink applications (e.g., 8.2–8.4 GHz). In future work, the following strategies can be adopted to broaden the axial ratio bandwidth: (1) using a multi-layer meta surface structure to increase the degrees of freedom in resonance; (2) designing a meta surface with multi-resonant or non-uniform unit cells; (3) introducing a wideband polarization converter. These approaches are expected to significantly enhance the operational bandwidth while maintaining circular polarization.

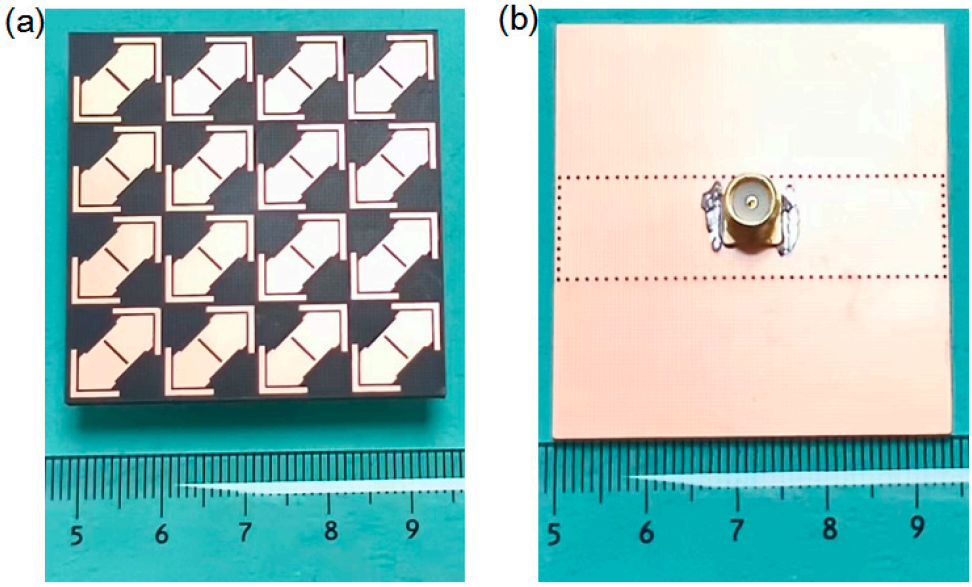


Figure 12. Front overall view of the antenna and the feeding port on the back side. (**a**) Physical dimension comparison of the staple-shaped structure on the antenna front side. (**b**) The back side of the antenna uses a coaxial cable feed.

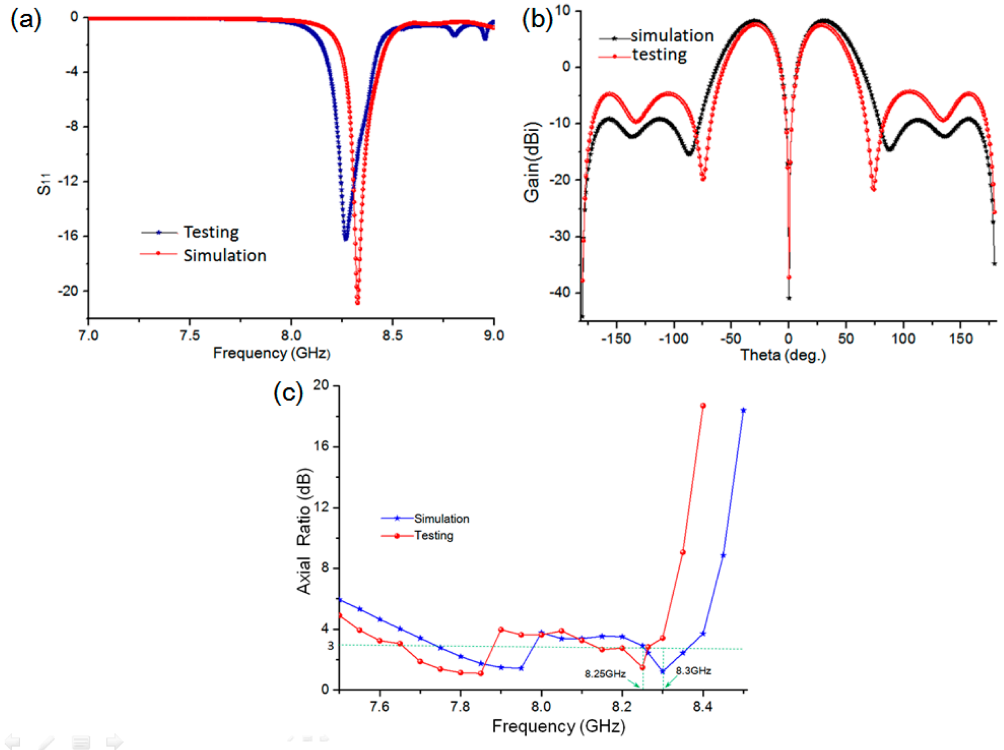


Figure 13. Comparison between measured data and simulated data. (**a**) The S_{11} of simulated and measured. (**b**) Simulated and measured E-plane patterns of the antenna. (**c**) Simulated and measured axial ratio of the antenna radiation.

Table 3 compares the proposed antenna with three representative ENZ-based single-beam, linearly polarized designs reported in the literature. It should be noted that these references operate over a wide frequency range (from 5.18 GHz to 29.5 GHz) and have different aperture sizes; therefore, a direct numerical comparison of absolute gain values across different frequencies is not strictly fair. Instead, the key message of Table 3 is to highlight the functional and architectural differences between prior works and this design.

Table 3. The comparison between this work and recent representative ENZ antennas.

Ref.	Functionality	Frequency (GHz)	Gain (dBi)	Feeding Components	Rad. Eff. (%)
[29]	Single-beam, linear	29.5	11	Substrate Integrated Cavity (SIC) + Grounded Coplanar Waveguide (GCPW)	about 80
[30]	Single-beam, linear	about 8	6.51	MEMS phase shifters	96
[31]	Single-beam, linear	5.18/5.72	10	Integrated SMA coaxial feed	58
This work	Dual-beam, CP	8.3	9.1	No phase shifter/divider	>85

Note: The compared references operate at different frequencies and have different aperture sizes; absolute gain values are not directly comparable across rows. The key comparison lies in the functional and architectural differences.

All compared references radiate a single beam with linear polarization, whereas the proposed antenna generates dual beams with circular polarization. More importantly, their feeding networks are significantly more complex. Reference [29] uses a Substrate Integrated Cavity (SIC) combined with a Grounded Coplanar Waveguide (GCPW) power divider; Reference [30] relies on MEMS phase shifters; and Reference [31] employs an integrated SMA coaxial feed. In sharp contrast, the proposed ENZ feeding network requires no phase shifters or power dividers whatsoever. This results in an excess insertion loss of only 0.9 dB, which is considerably lower than typical Butler matrices (2–4 dB).

In terms of gain, the proposed design achieves 9.1 dBi at 8.3 GHz, which is comparable to or higher than the gain of [30] (6.51 dBi at ≈8 GHz) and moderate compared to [29] (11 dBi at 29.5 GHz) and [31] (10 dBi at 5.18/5.72 GHz). The lower gain of [30] is mainly due to its electrically small aperture. The radiation efficiency of the proposed antenna (>85%) is competitive, especially considering the additional polarization-conversion layer.

Overall, the comparison in Table 3 demonstrates that the proposed antenna offers a unique combination of dual-beam circular polarization and a low-complexity, low-loss feeding network—a feature set that is not simultaneously available in any of the prior ENZ antennas. This makes it attractive for compact satellite terminals and small base stations where both spatial coverage and system efficiency are critical.

6. Conclusions

This paper presents a low-loss, highly integrated dual-beam circularly polarized antenna array using an SIW-based ENZ feeding network. By investigating the field characteristics in slotted SIW structures under the ENZ mode, this work verifies that the tangential electric field in the radiating slots presents an equal-amplitude and anti-phase distribution, which is generated by the uniform field property of the ENZ medium and the boundary constraint of the slotted PEC surface. Based on this inherent mechanism, symmetric dual-beam radiation can be realized directly without additional phase shifters, power dividers, or complex beamforming networks. A three-layer integrated configuration is designed, including the ENZ feeding layer, radiating layer, and polarization conversion meta surface layer, which realizes low-profile, high-efficiency circularly polarized dual-beam radiation.

The proposed antenna is fabricated and measured. At the operating frequency of 8.3 GHz, the prototype achieves a peak gain of 9.1 dBi, a minimum axial ratio lower than 1.5 dB, and a radiation efficiency higher than 85%. The dual beams are symmetric with good directivity, and the overall structure features compact size, low loss, and high integration. Compared with conventional dual-beam circularly polarized antenna arrays, the proposed design avoids complex feeding networks and achieves improved radiation efficiency and integration.

The proposed antenna and design method show good potential for application in satellite communication terminals and compact base stations. Furthermore, the revealed field distribution mechanism can be extended to the design of multi-beam, high-gain, and low-loss antenna arrays for microwave and millimeter-wave wireless communication systems.

It is worth noting that the revealed anti-phase tangential-field mechanism is scale-dependent and can be naturally extended to millimeter-wave bands by proportionally scaling the SIW structure and slot dimensions, offering a promising route to low-complexity multi-beam CP antenna arrays at millimeter-wave frequencies.

Author Contributions: Conceptualization, D.L.; Methodology, R.H.; Validation, D.L.; Data curation, R.H.; Writing—original draft, D.L.; Writing—review & editing, R.H.; Supervision, D.L.; Project administration, D.L.; Funding acquisition, R.H. All authors have read and agreed to the published version of the manuscript.

Funding: This research was funded by the Natural Science Foundation of Hubei Province of China (2022CFB421).

Institutional Review Board Statement: Not applicable.

Informed Consent Statement: Not applicable.

Data Availability Statement: The original contributions presented in this study are included in the article. Further inquiries can be directed to the corresponding authors.

Conflicts of Interest: The authors declare no conflict of interest.

References

1. Qin, Y.; Han, M.; Zhang, L.; Mao, C.X.; Zhu, H. A Compact Dual-Band Omnidirectional Circularly Polarized Filtering Antenna for UAV Communications. *IEEE Trans. Veh. Technol.* **2023**, *72*, 16742–16747. [CrossRef]
2. Ye, K.; Lu, Y.; You, Q.; Wang, K.; Xu, J.; Huang, J. Compact Dual-Band Shared-Aperture Omnidirectional Biconical Antenna for Microwave and Millimeter-Wave Applications. *IEEE Trans. Antennas Propag.* **2024**, *72*, 4594–4599. [CrossRef]
3. Li, J.; Zhao, L.; Wu, H. A Novel Highly Directional Antenna Array Based on Epsilon-Mu-Near-Zero (EMNZ) with Air Gap Structure. *IEEE Trans. Antennas Propag.* **2025**, *73*, 2357–2358. [CrossRef]
4. Chen, P.; Zhao, Y.; Yang, X.; Guo, R.Y.; Li, Y.; Ge, L. High-Gain Omnidirectional Transmitarray Antenna. *IEEE Trans. Antennas Propag.* **2023**, *71*, 8441–8449. [CrossRef]
5. Chen, D.; Xue, Q.; Yang, W.; Chin, K.S.; Jin, H.; Che, W. A Compact Wideband Low-Profile Meta surface Antenna Loaded with Patch-Via-Wall Structure. *IEEE Antennas Wirel. Propag. Lett.* **2023**, *22*, 179–183. [CrossRef]
6. Abdulkarim, Y.I.; Awl, H.N.; Muhammadsharif, F.F.; Karaaslan, M.; Mahmud, R.H.; Hasan, S.O.; Işık, Ö.; Luo, H.; Huang, S. A Low-Profile Antenna Based on Single-Layer Meta surface for Ku-Band Applications. *Int. J. Antennas Propag.* **2020**, *2020*, 8813951. [CrossRef]
7. Yang, G.; Li, J.; Zhou, S.G.; Qi, Y. A Wide-Angle E-Plane Scanning Linear Array Antenna with Wide Beam Elements. *IEEE Antennas Wirel. Propag. Lett.* **2017**, *16*, 2923–2926. [CrossRef]
8. Yang, G.; Zhang, S. Dual-Polarized Wide-Angle Scanning Phased Array Antenna for 5G Communication Systems. *IEEE Trans. Antennas Propag.* **2022**, *70*, 7427–7438. [CrossRef]
9. Xu, F.; Wu, K. Guided-wave and leakage characteristics of substrate integrated waveguide. *IEEE Trans. Microw. Theory Tech.* **2005**, *53*, 66–73. [CrossRef]
10. Rotman, W. Plasma simulation by artificial dielectrics and parallel-plate media. *IEEE Trans. Antennas Propag.* **1962**, *10*, 82–95. [CrossRef]
11. Chang, L.; Li, Y.; Zhang, Z.; Feng, Z. Horizontally Polarized Omnidirectional Antenna Array Using Cascaded Cavities. *IEEE Trans. Antennas Propag.* **2016**, *64*, 5454–5459. [CrossRef]
12. Haghparast, A.; Rezaei, P.; Zilouchian, A. Compact triple—Band ring-shaped printed antenna with circular polarization. *J. Electromagn. Waves Appl.* **2025**, *39*, 158.
13. Al Ka'Bi, A. A Dual-Band Microstrip Antenna Array with Enhanced Circular Polarization for 6G Systems. *Wirel. Pers. Commun.* **2025**, *145*, 335–355. [CrossRef]
14. Wang, Z.; Zhao, S.; Dong, Y. Metamaterial-Based Wide-Beam Dielectric Resonator Antenna for Broadband Wide-Angle Beam-Scanning Phased Array Applications. *IEEE Trans. Antennas Propag.* **2022**, *70*, 9061–9072. [CrossRef]

15. Zhang, Y.; Li, H.; Zhao, Y.; Li, Y. 2-D Epsilon-Near-Zero (ENZ) Feeding Network for High-Gain Millimeter-Wave Slot Antenna Array Using Bulk Silicon MEMS Technology. *IEEE Trans. Antennas Propag.* **2024**, *72*, 3055–3063. [CrossRef]
16. Li, H.; Zhou, Z.; Zhao, Y.; Li, Y. Low-loss beam synthesizing network based on epsilon-near-zero (ENZ) medium for on-chip antenna array. *Chip* **2023**, *2*, 100049. [CrossRef]
17. George, D.M.; Chandroth, A. 5 GHz high gain slotted SIW epsilon near zero antenna array for wireless communications. *Eng. Res. Express* **2020**, *2*, 45014. [CrossRef]
18. Liu, Z.; Jens, B.; Liu, S.; Kong, X. Investigations and prospects of Fabry-Perot antennas: A review. *J. Syst. Eng. Electron.* **2021**, *32*, 731–747. [CrossRef]
19. Zhou, L.; Duan, X.; Luo, Z.; Zhou, Y.; Chen, X. High Directivity Fabry–Perot Antenna with a Nonuniform Partially Reflective Surface and a Phase Correcting Structure. *IEEE Trans. Antennas Propag.* **2020**, *68*, 7601–7606. [CrossRef]
20. Jeon, Y.G.; Yun, G.R.; Kim, J.; Kim, D. Polarization Reconfigurable High-Gain Fabry–Perot Cavity Antenna. *IEEE Trans. Antennas Propag.* **2022**, *70*, 7727–7734. [CrossRef]
21. Zhou, Z.; Li, Y.; He, Y.; Zhang, Z.; Chen, P.Y. A Slender Fabry–Perot Antenna for High-Gain Horizontally Polarized Omnidirectional Radiation. *IEEE Trans. Antennas Propag.* **2021**, *69*, 526–531. [CrossRef]
22. Hussain, N.; Jeong, M.J.; Park, J.; Kim, N. A Broadband Circularly Polarized Fabry-Perot Resonant Antenna Using A Single-Layered PRS for 5G MIMO Applications. *IEEE Access* **2019**, *7*, 42897–42907. [CrossRef]
23. Liu, Z.; Zhang, Y.; Sun, W.; Li, Y. Low-Profile Epsilon-Near-Zero (ENZ) Cavity Antenna Array for Wide-Angle Beam Scanning. *IEEE Antennas Wirel. Propag. Lett.* **2024**, *23*, 2115–2119. [CrossRef]
24. Dadgarpour, A.; Sorkherizi, M.S.; Denidni, T.A.; Kishk, A.A. Passive Beam Switching and Dual-Beam Radiation Slot Antenna Loaded with ENZ Medium and Excited Through Ridge Gap Waveguide at Millimeter-Waves. *IEEE Trans. Antennas Propag.* **2017**, *65*, 92–102. [CrossRef]
25. Oh, Z.X.; Yeap, K.H.; Teh, P.C. Circular split-ring resonator-based sensor for dielectric constant measurement. *Microw. Opt. Technol. Lett.* **2023**, *65*, 513–518.
26. Inclan Alonso, J.M.; Amazares Calderon, G.; Sierra Perez, M. SIW Antenna with Polarizer at ku-Band. *IEEE Trans. Antennas Propag.* **2015**, *63*, 2782–2786. [CrossRef]
27. Che, W.Q.; Xu, L.; Wang, D.P.; Geng, L.; Deng, K.; Chow, Y.L. Short-Circuit equivalence between rectangular waveguides, of regular sidewalls(RW)and of sidewalls of cylinders(SIRW), plus its extension to cavity. *IET Microw. Antennas Propag.* **2007**, *1*, 639–644. [CrossRef] [PubMed]
28. Yang, W.; Chen, S.; Che, W.; Xue, Q.; Meng, Q. Compact High-Gain Meta surface Antenna Arrays Based on Higher-Mode SIW Cavities. *IEEE Trans. Antennas Propag.* **2018**, *66*, 4918–4923. [CrossRef]
29. El-Nady, S.; Elsharkawy, R.R.; Afifi, A.I.; Abd El-Hameed, A.S. Performance Improvement of Substrate Integrated Cavity Fed Dipole Array An-tenna Using ENZ Metamaterial for 5G Applications. *Sensors* **2021**, *22*, 125. [CrossRef] [PubMed]
30. Dash, R.K.; Kumari, S.; Choudhury, B. Novel high-gain narrowband antenna based on ENZ SIW structure and shorting pin. *Analog. Integr. Circuits Signal Process.* **2024**, *119*, 455–462. [CrossRef]
31. Li, J.; Zhao, L.; Long, D. Xie Low-Profile Omnidirectional and Wide-Angle Beam Scanning Antenna Array Based on Epsilon-Near-Zero and Fabry–Perot Co-Resonance. *Electronics* **2025**, *14*, 2012.

Disclaimer/Publisher's Note: The statements, opinions and data contained in all publications are solely those of the individual author(s) and contributor(s) and not of MDPI and/or the editor(s). MDPI and/or the editor(s) disclaim responsibility for any injury to people or property resulting from any ideas, methods, instructions or products referred to in the content.